Enhancement of Oxygen Transfer by Design Nickel Foam Electrode for Zinc−Air Battery

Ke Xu,[1] Adeline Loh,[2] Baoguo Wang,[1,z] and Xiaohong Li[2]

[1]*Department of Chemical Engineering, Tsinghua University, Beijing 100084, People's Republic of China*
[2]*Renewable Energy Group, College of Engineering, Mathematics and Physical Sciences, University of Exeter, Cornwall TR10 9FE, United Kingdom*

To develop a long-lifetime metal-air battery, oxygen reduction electrodes with improved mass-transfer routes are designed by adjusting the mass ratio of the hydrophobic polytetrafluoroethylene (PTFE) to carbon nanotubes (CNTs) in nickel foam. The oxygen reduction catalyst MnO_2 is grown on the nickel foam using a hydrothermal method. Scanning electron microscopy, X-ray diffraction, X-ray photoelectron spectroscopy, and Brunauer–Emmett–Teller analysis are employed to characterize the morphology, crystal structure, chemical composition, and pore structure of the electrodes, respectively. The air electrodes are evaluated using constant-current tests and electrochemical impedance spectroscopy. A PTFE:CNT mass ratio of 1:4–2:1 with 3-mm-thick nickel foam yields the optimal performance due to the balance of hydrophilicity and hydrophobicity. When the electrodes are applied in primary zinc–air batteries, the electrode with a PTFE:CNT mass ratio of 1:4 achieves the maximum power density of 95.7 mW cm^{-2} with a discharge voltage of 0.8 V at 100 mA cm^{-2}, and completes stable discharge for over 14400 s at 20 mA cm^{-2}.
 [DOI: 10.1149/2.0361805jes]

Manuscript submitted December 19, 2017; revised manuscript received March 5, 2018. Published March 21, 2018.

Growing global interest in the development of a smart grid and electric vehicles requires long-lifetime, cost-effective, and environmentally friendly batteries, such as zinc–air and lithium–air batteries. Metal–air batteries offer beneficial properties, such as high theoretical energy and power densities, low operating temperature, low cost, and material recyclability.[1] In particular, metal–air batteries offer an advantage over other batteries in that the cathode electroactive species (oxygen) is not stored in the battery system but supplied from the surrounding environment during the discharge process. This unique nature simplifies the metal–air battery structure, which leads to a lighter and more compact battery, thereby increasing the specific energy, which approaches 470 and 1700 Wh kg^{-1} for zinc−air and lithium−air batteries, respectively.[2]

The oxygen reaction electrode is the core component of metal–air batteries, where the oxygen is reduced through multistep electron transfer processes, involving complicated oxygen-containing species such as O, OH, O_2^{2-}, HO_2^-.[3–6] It is generally accepted that oxygen reduction may proceed via a four-electron pathway or two-electron pathway. The specific reactions of oxygen reduction reaction (ORR) in alkaline media are as followings:

1. In a four-electron pathway, O_2 is reduced to OH^-;

$$O_2 + 2H_2O + 4e^- \leftrightarrow 4OH^-;\ E^0 = 0.401\ V\ vs\ SHE \quad [1]$$

2. In a two-electron pathway, O_2 is reduced to peroxide ion followed by either further reduction or disproportionation.

$$O_2 + H_2O + 2e^- \leftrightarrow HO_2^- + OH^-;\ E^0 = -0.076\ V\ vs\ SHE \quad [2]$$

$$HO_2^- + H_2O + 2e^- \leftrightarrow 3OH^-;\ E^0 = 0.878\ V\ vs\ SHE \quad [3]$$

$$2HO_2^- \leftrightarrow 2OH^- + O_2 \quad [4]$$

The oxygen reduction reaction (ORR) is usually kinetically sluggish relative to the negative metal anode in these batteries, which results in great voltage loss in the ORR cathode and limits battery performance. This behavior can be partially attributed to the low solubility of O_2 of 1.25 mM in aqueous solutions,[7] and 10^{-4} mM in 30 wt% KOH at 25°C,[8] which makes it difficult for oxygen to adsorb on the surface of catalysts in the cathode.[9] Oxygen has an exceptionally high bond energy of 498 kJ mol^{-1}, which is far larger than that of other chemical species in the battery system, thus leading to poor kinetics for the ORR process. Therefore, developing a highly active ORR electrode is a priority to help overcome the barrier that constrains the performance improvement of metal–air batteries.

The development of a highly active electrocatalyst is an effective strategy to improve the reaction kinetics and decrease the overpotential associated with the ORR, which greatly limit the performance of metal–air batteries.[10–17] Significant progress has been made in the development of ORR catalysts, including transition-metal-based materials (oxides,[16,18–20] sulfides,[21] chalcogenides,[22] nitrides,[14,23] and carbides),[24] heteroatom-doped carbon nanomaterials,[25,26] and hybrid materials.[27–29] An air electrode is generally composed of a gas diffusion layer, current collector, and catalyst layer. Highly active catalysts are usually mixed with polytetrafluoroethylene (PTFE) and carbon materials to prepare the catalyst layer. By spraying[30,31] or drop casting[28,32–34] the catalyst ink, the ORR cathode can be obtained in combination with the current collector and gas diffusion layer. Because of the weak physical interaction between the catalyst and current collector, the catalysts can be easily detached, resulting in performance decay of metal−air batteries. Moreover, the entire process is complex, many active sites of catalysts are easily buried, and the multilayer design results in poor electron transfer properties, which generally limit the utilization of nanostructured electrocatalysts.

To provide high accessibility of active sites and a low interfacial contact resistance, some novel integrative designs for air electrodes have been proposed including the growth of nanostructured catalysts on porous substrates (e.g., carbon cloths, metal meshes/foams) using chemical vapor deposition,[35] electrodeposition,[36] pulsed laser deposition,[37] and electrospinning.[38] The substrate in the integrative electrode plays the role of both the current collector and catalyst support. Recently, Fu et al.[35] reported the direct growth of Co_3O_4/nitrogen-doped carbon nanotubes (NCNTs) on stainless steel mesh as an integrative air electrode used in zinc–air batteries. The Co_3O_4/NCNTs exhibited comparable ORR activity to that of Pt/C catalysts sprayed on stainless steel mesh. The superior performance of the electrode was thought to mainly arise from the advanced electrode design and strong coupling between Co_3O_4 and the NCNTs. Ma et al.[37] fabricated a flexible oxygen electrode of phosphorus-doped graphitic carbon nitride (P-g-C_3N_4) grown in situ on carbon fiber paper, which exhibited outstanding activity and stability for the ORR and oxygen evolution reaction. This performance was derived from the intimate interfacial contact between the P-g-C_3N_4 and carbon fiber paper, which facilitated the electron transfer between the two components.

[z]E-mail: bgwang@tsinghua.edu.cn

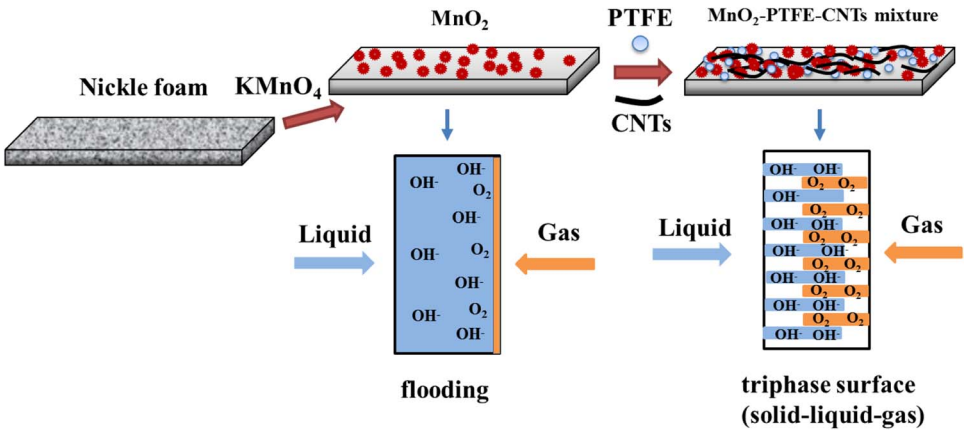

Figure 1. Schematic diagrams of the fabrication of the 3D oxygen electrode and the corresponding interface process.

Despite the efforts made in the development of integrative oxygen electrodes,[35,37–48] most of these studies have focused on the exploitation of new catalysts, whereas efforts to investigate the mass-transfer structure of the porous electrode are currently lacking. Oxygen reduction is a typical triphase reaction process, involving oxygen from the gas phase, hydroxide from the aqueous solution, and electron conduction in the solid, with charge transfer occurring at the triphase interfaces (liquid–gas–solid interfaces). Compared with hydroxide ion diffusion and electron conduction, oxygen transfer is usually the "bottleneck" because of the low solubility of oxygen in aqueous solution. Flooding in the cathode impedes oxygen transport to reaction sites and seriously blocks the surface of the catalysts, thereby resulting in a significant, sometimes catastrophic, decrease in battery performance. For this reason, fabrication of a gas diffusion route through the ORR cathode becomes a critical issue in theoretical investigations of integrative electrode design.[49–52] To prevent flooding of the oxygen diffusion route, balance is required between hydrophilicity and hydrophobicity. The hydrophilic channels in the electrode must be appropriately wetted to provide access to the liquid electrolyte, and the hydrophobic channels must be designed to facilitate oxygen transfer from the atmosphere to the active sites and to avoid leakage. To our knowledge, there is little research on the effect of the cathode structure and oxygen transfer route on zinc–air battery performance or a guide to help maintain the balance of the 3D interfacial surface for ORR cathode design.

In this study, the oxygen reduction catalyst MnO_2 was directly grown on nickel foam using hydrothermal method. As reported in literature, MnO_2 exhibits considerable electrocatalytic activity and possesses advantages such as low toxicity, low cost, and environmental friendliness.[53–58] Recently, Meng studied the structure-property relationship of manganese oxides with different crystal structures, and found that α-MnO_2 was more active than other structures for ORR.[59] Cheng discovered a facile strategy to enhance the activity of β-MnO_2 by introducing native oxygen defects into the manganese oxides, which enabled larger current, and lower peroxide yield for the ORR electrocatalysis.[60] Among different manganese oxides, layered manganese dioxide (δ-MnO_2), consisting of edge sharing MnO_6 octahedra, demonstrates excellent water oxidation and oxygen reduction reaction performance, as can be seen in many investigations.[53,56,61,62]

To achieve a balance of hydrophilic/hydrophobic interaction, the hydrophobic components PTFE and carbon nanotubes (CNTs) were added to Ni foam coated with MnO_2 using hydrothermal synthesis. Oxygen transfer channels were fabricated by adjusting the mass ratio of PTFE to CNTs (FT9000, Cnano Technology Ltd. Beijing, China). The electrochemical performance of the electrodes was tested using a three-electrode system for the zinc–air battery discharge process. Finally, the enhanced oxygen transfer effects with an appropriate ratio of hydrophilic to hydrophobic components were discussed in detail. Schematic diagrams of the fabrication of the 3D oxygen electrode and the corresponding interface process are presented in Fig. 1.

Experimental

Synthesis of MnO_2 nanospheres on ni foam.—All chemical reagents were of analytical purity and used without any further purification. MnO_2 nanospheres were directly grown on nickel foam via a modified hydrothermal method.[63] The Ni foam (3 × 7 cm, 5-mm thick, Shenzhen Lifeixin Environmental Protection Co., Ltd) was soaked in 3 M HCl (Beijing Modern Oriental Fine Chemistry Co., Ltd.) for 30 min and rinsed with deionized water and ethanol under ultrasonication for several minutes. Five pieces of Ni foam were placed against the wall of a 200-mL Teflon-lined autoclave containing a homogenous solution of $KMnO_4$ (1 g, Beijing Modern Oriental Fine Chemistry Co., Ltd.) in 120 mL of deionized water. After reaction at 160°C for 24 h, the substrates coated with MnO_2 nanospheres were removed and washed with deionized water under ultrasonication and rinsed with ethanol to remove physisorbed and loosely attached MnO_2, followed by drying at 80°C overnight. The loading density of MnO_2 was calculated to be approximately 4.0 mg cm^{-2}.

Fabrication of Ni/MnO_2 air electrodes.—The Ni/MnO_2 electrodes were coated with a gas diffusion layer, which was prepared using CNTs (0.5 g, FT9000, Cnano Technology Ltd. Beijing, China) and a PTFE emulsion (60 wt%, Shanghai Hesen Electric Co., Ltd) with PTFE:CNT mass ratios of 0:1, 1:2, 1:1, 2:1, 4:1, 6:1, 8:1, and 10:1 in 15 mL of absolute ethanol. This mixture was stirred for approximately 30 min, ultrasonically separated for 30 min, and heated in a water bath for approximately 10 min at 80°C. The gas diffusion layer was fitted on one side of Ni/MnO_2, and a Teflon membrane was attached to the back side of the electrode. Finally, the air electrode was pressed into a 0.4-mm-thick layer under a pressure of 30 MPa and then dried at 80°C for 12 h. The schematic diagram of the air electrode structure is shown in Fig. 2.

Material characterization.—Morphological investigation was performed using scanning electron microscopy (SEM, Merlin, Carl Zeiss, Germany). The chemical compositions of the electrodes were determined using energy-dispersive X-ray spectroscopy (EDS, Merlin, Carl Zeiss, Germany), and X-ray diffraction (XRD, Bruker D8 Advance, Bruker, Germany) was used to analyze the crystal structure of the catalysts with continuous scanning in the diffraction angle range (2θ) of 10°–80°. X-ray photoelectron spectroscopy (XPS) was performed on an ESCALAB 250Xi (Thermo Fisher, England) using Al Kα radiation as the radiation source. All the binding energies are referenced to the C 1 s peak at 284.8 eV. N_2 adsorption-desorption isotherms were measured at 77 K with an IQ2 sorptometer (Quantachrome Instruments, USA). The specific surface area was

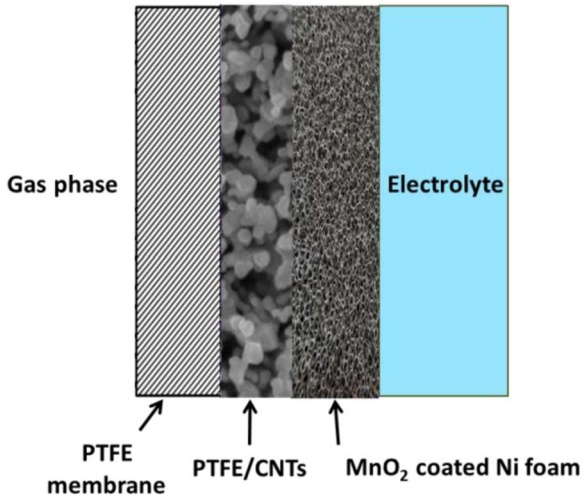

Figure 2. The schematic diagram of the air electrode structure.

calculated using the Brunauer–Emmett–Teller (BET) equation, and the pore size distribution was calculated from the adsorption curve using the Barrett–Joyner–Halenda (BJH) method.

Electrochemical measurements.—*Electrochemical activity.—* Electrochemical tests were performed in 6 M KOH using an electrochemical workstation (VersaSTAT-3, Princeton Applied Research, USA) with a three-electrode set-up. A saturated calomel electrode and platinum mesh were used as the reference electrode and counter electrode, respectively. The Ni/MnO_2 cathode coated with a mixture of PTFE and CNT was directly used as the working electrode with a geometric working area of 1 cm^2. The electrochemical activity was evaluated using galvanostatic discharge and electrochemical impedance spectroscopy (EIS). The electrodes were tested at current densities of 0, 5, 10, 20, and 30 mA cm^{-2}. Potentiostatic EIS was conducted at an ORR potential of −0.3 V vs. Hg/HgO with an amplitude of 10 mV in the frequency range of 100 kHz to 0.1 Hz to obtain Nyquist plots. The electrochemical active surface area was analyzed using double-layer capacitance (C_{dl}) tests. Cyclic voltammetry (CV) curves were measured in a potential window nearly without any faradaic processes at scan rates of 1, 1.5, 2, 2.5, and 3 mVs^{-1} for oxygen reduction electrodes with different mass-transfer structures.

Zinc–air battery.—A polished zinc plate (Institute of Metal Research, Beijing, China) and air electrode were used as the anode and cathode, respectively. The geometric area of the cathode exposed to air was approximately 1 cm^2, and the same area of the catalyst layer was exposed to the electrolyte (6 M KOH). Constant-current discharge measurements were conducted to estimate the electrochemical performance of the air electrode applied in a zinc–air battery. The measurement was performed using the same electrochemical workstation as the three-electrode system under the ambient air atmosphere.

Results and Discussion

Morphology, crystal structure, and chemical composition.—The morphology of the MnO_2 nanospheres directly grown on Ni foam was examined using SEM. Figs. 3a and 3b present representative SEM images of the Ni foam and MnO_2 nanospheres on the Ni foam, respectively. The 3D grid structure with hierarchical macroporosity of the pristine Ni foam was still observed for the MnO_2 nanospheres grown on Ni foam. The insets in Figs. 3a and 3b present magnified SEM images of the Ni foam and MnO_2 nanospheres on Ni foam, respectively, further revealing their microstructures. For the MnO_2 grown on Ni foam, the skeleton of the Ni foam was generally completely and uniformly covered by MnO_2 nanosheets assembled into nanospheres. This structure was considerably different from that of the pristine Ni foam, which exhibited no surface covering. Here, the Ni foam serves as both the current collector and catalyst substrate. The 3D network structure formed by the MnO_2 nanospheres and Ni foam substrate, with micro open cages and zigzag flow channels, provided the electrode with a mass transport property for the diffusion of O_2 and facilitated ion diffusion during the catalytic process. The MnO_2 on the Ni foam contained Ni, Mn, and O as the main components according to the EDS analysis. The elemental mappings revealed that Mn and O mainly occupied the positions of the nanospheres, with Ni primarily distributed in the crevices, and these elements had a relatively homogeneous distribution throughout the entire region (Figs. 3c, 3d, 3e, 3f). Fig. 3g presents an XRD pattern of the MnO_2 directly grown on Ni foam. Excluding the strong peaks from the Ni foam, diffraction peaks were detected for MnO_2 at 12.52°, 25.12°, and 36.94°, which could be assigned to the (001), (002), and (−111) planes of the birnessite-type manganese oxide crystal (JCPDS 80-1098, a = 5.149 Å, b = 2.843 Å, c = 7.716 Å). This result agrees well with the reported structure for δ-MnO_2 on Ni foam.[61,63]

XPS was used to probe the chemical states of Mn and O on the electrode surface. Fig. 3h presents the XPS spectrum of the Mn 2p signal. The peaks of Mn $2p_{1/2}$ and Mn $2p_{3/2}$ were centered at 654.0 and 642.5 eV, respectively, with a spin energy of 11.5 eV; these values are consistent with previously reported data.[61,64] Deconvoluted Mn $2p_{3/2}$ peaks at 642.6 and 641.8 eV are attributed to the presence of Mn^{4+} and Mn^{3+} oxide phases, respectively.[65–67] The amount of Mn^{4+} and Mn^{3+} oxide phases is determined to be 94% and 6%, respectively, which indicates that the dominated oxidation state of manganese oxide in the composites is tetravalent oxide. In addition, the presence of Mn^{3+} leads to better electrocatalytic performance due to oxygen defects in the material.[59–61] Fig. 3i presents the fitted O 1 s spectrum, which contains one sharp peak at 530 eV and two broad peaks at 531.6 and 532.6 eV. The first two peaks were attributed to the oxygen atoms bound to Mn atoms in higher and lower oxidation states represented by Mn–O–Mn or Mn–O–H bond configurations, respectively. The peak at 532.6 eV was assigned to oxygen from water molecules (H–O–H bonds). The manganese oxidation state could be determined from the O 1 s spectra. The average oxidation states of Mn can be determined from the intensities of the Mn–O–Mn and Mn–O–H components according to the next equation[59,68]

$$O_x State = \frac{IV * (S_{M-O-Mn} - S_{Mn-O-H}) + III * S_{Mn-O-H}}{S_{Mn-O-Mn}}$$

where $S_{Mn\text{-}O\text{-}Mn}$ represents the contribution from both MnOOH and MnO_2, whereas $S_{Mn\text{-}O\text{-}H}$ stands for the contribution from hydroxyl groups. III and IV refer to Mn(III) and Mn(IV) with numerical values of 3 and 4, respectively.[69] The average oxidation state of Mn on Ni foam was calculated to be 3.88, which is consistent with the deconvoluted results of Mn2p.

Fabrication of gas diffusion channel with different mass ratios of PTFE to CNTs.—*Morphology changes with different mass ratios of PTFE to CNTs.—*To adjust the mass-transfer structure of the electrode, different mass ratios of PTFE to CNTs were fitted on Ni/MnO_2. Here, the MnO_2 and Ni foam provide the hydrophilic channels, which give access to the liquid electrolyte, and the mixture of PTFE and CNTs serves as the hydrophobic channels that promote the oxygen transport within the triphase zone. The electrode maintains an effective porosity, improved mass transfer, and more effective water management because of its structural advantages. Figs. 4a, 4b, 4c, 4d shows the morphology of the gas diffusion layer with different mass ratios of PTFE to CNTs. As can be seen in Figs. 4a, 4b, 4c, 4d, the sample with a PTFE:CNT mass ratio of 1:2 was more loose than the other samples. With increasing PTFE content, the surface structure became more compact, as observed in the low-magnification SEM images. From the high-magnification images, the samples with mass

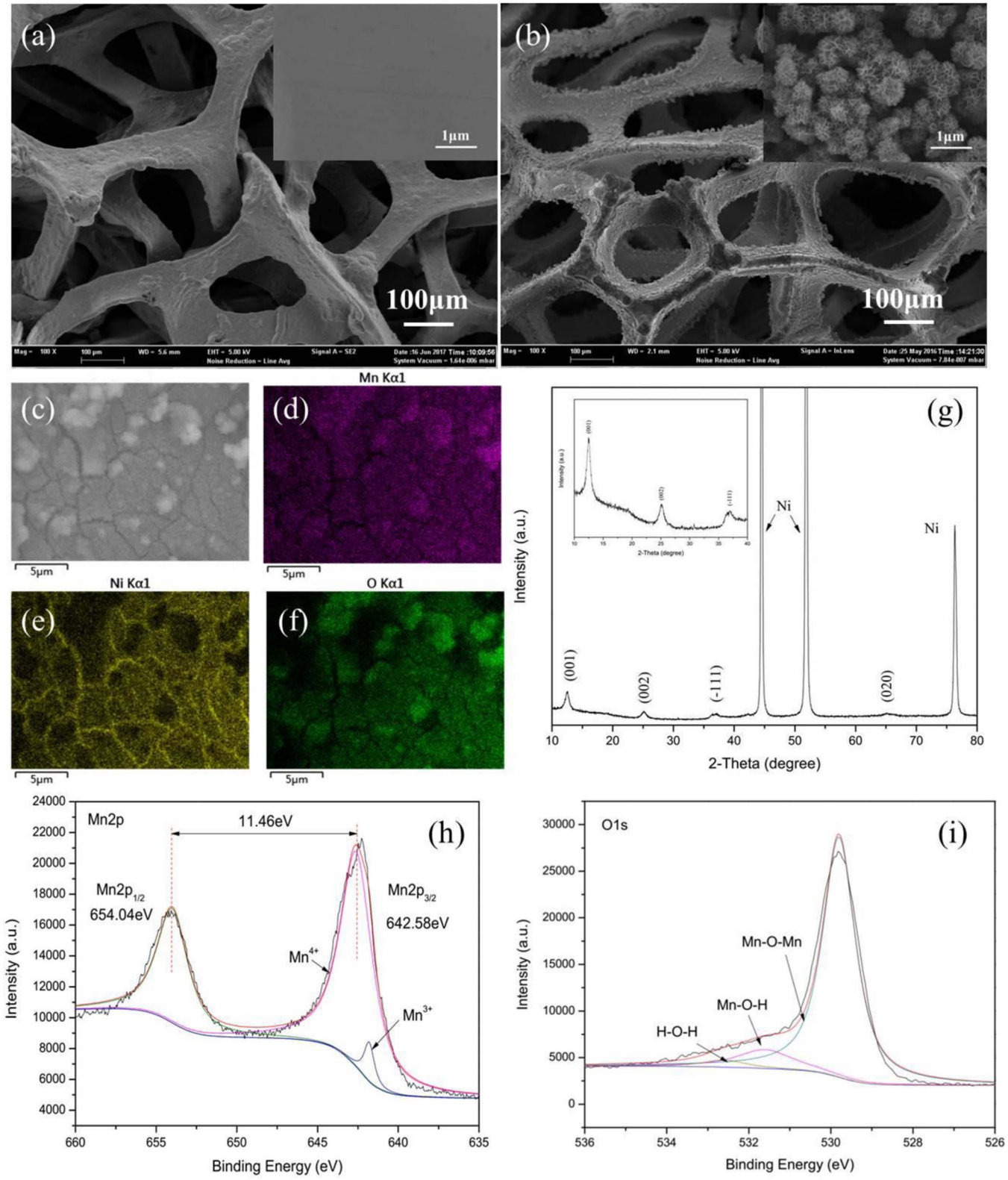

Figure 3. (a) SEM images of Ni foam and (b) MnO_2-coated Ni foam. The insets present high-magnification images. (c) SEM image used for EDS analysis and EDS elemental mappings of (d) Mn, (e) Ni, and (f) O distributions. (g) XRD pattern of MnO_2-coated Ni foam. The inset presents a magnified view of the range of 10–40°. XPS spectra of (h) Mn 2p and (i) O 1 s.

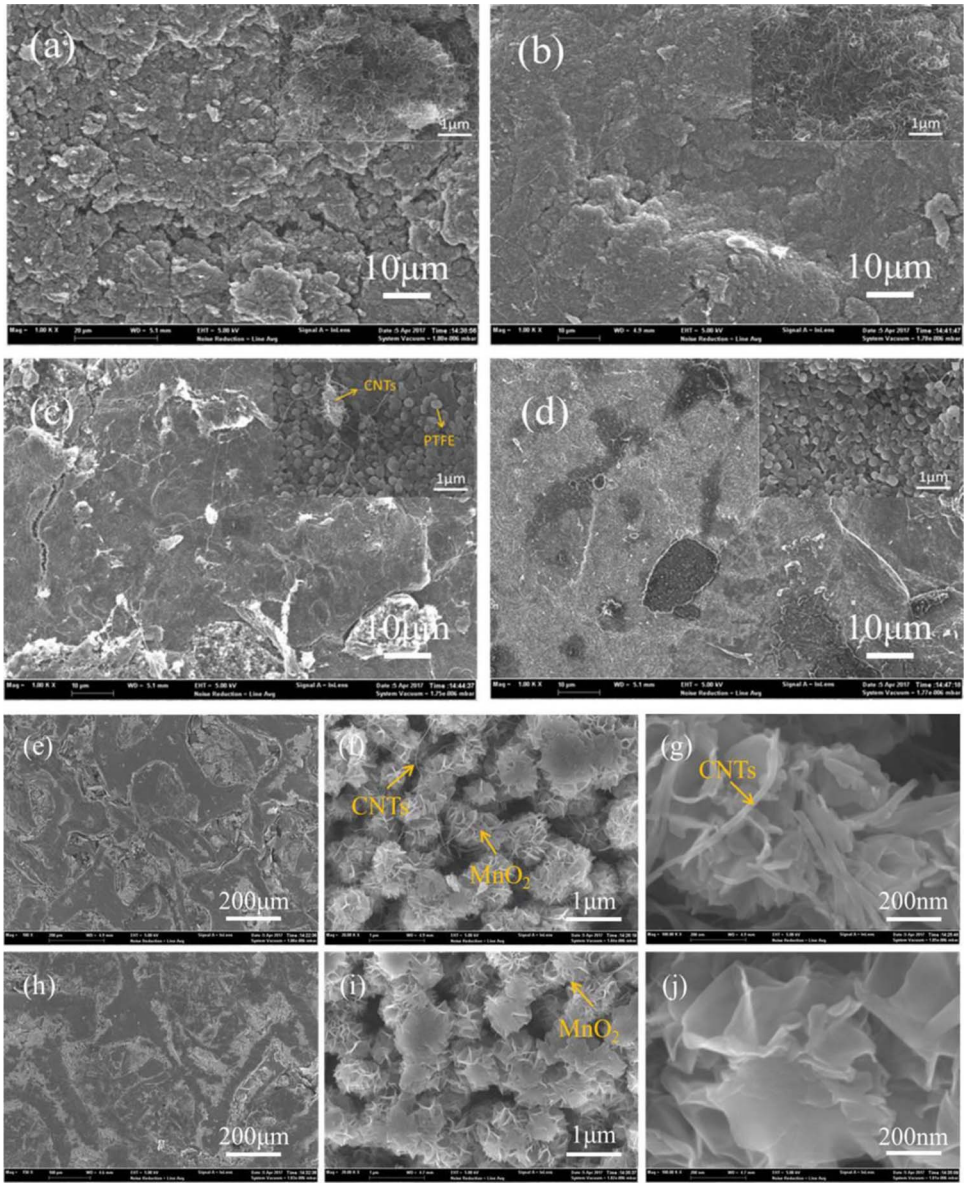

Figure 4. SEM images of gas diffusion layer for PTFE to CNT mass ratios of (a) 1:2, (b) 2:1, (c) 6:1, and (d) 8:1. The insets present high-magnification images. SEM images of the surface of air cathode facing electrolyte side for PTFE:CNT mass ratios of (e, f, g) 1:2 and (h, i, j) 8:1 at various scales.

ratios of 1:2 and 2:1, 6:1, and 8:1 consisted of only agglomerates of CNTs, agglomerates of CNTs and spherical PTFE particles, and mostly spherical PTFE particles, respectively.

Surface morphology of Ni/MnO_2 with different mass transfer structures.—The surface morphologies of Ni/MnO_2 coated with different mass ratios of PTFE to CNTs are displayed in Figs. 4e, 4f, 4g, 4h, 4i, 4j. Figs. 4e, 4f, 4j presents SEM images of Ni/MnO_2 with PTFE:CNT mass ratio of 1:2 (Ni/MnO_2-1:2). The 3D porous structure of the Ni foam can still be observed in Fig. 4e, and the CNTs have intimate contact with the MnO_2 nanospheres. The sample with the PTFE:CNT mass ratio of 8:1 had a more compact surface than that with the mass ratio of 1:2, as observed in Figs. 4i, 4j. The surface of this sample mainly consisted of MnO_2 nanospheres, with no visible CNTs. MnO_2 is known to exhibit poor conductivity; therefore, the intimate contact with the CNTs can improve the electrical contact. The Ni/MnO_2-1:2 sample contained more CNTs on the surface, which increased its conductivity. In addition, the large area of interfaces between MnO_2 nanospheres and CNTs generated a high population of active sites, promoting the ORR activity of the electrode via a synergistic effect.[45,70–72]

Stabilization of ORR electrode performance with addition of PTFE/ CNT mixtures.—The stabilization of ORR electrode performance was investigated by the electrochemical behaviors of the Ni foam electrode with or without the mixture of PTFE/CNTs. Using oxygen from ambient air in atmosphere, Fig. 5 shows the potential variation with time measured with two Ni foam electrodes, i) composed of MnO_2 covered on Ni foam; ii) covered by the mixture of PTFE/CNT (ratio 1:2) above MnO_2 layer. The latter gives better stability as showed in the different potential step corresponding to various current densities at 5, 10, 20 mA cm^{-2}. As a contrast, the former provides continuous decreasing potential, it can be ascribed to oxygen concentration decrease with time due to water clogging in the microspores of the electrode. This result illustrates the importance of appropriate balance of hydrophobic/ hydrophilic force in the porous structure of air electrode, the addition of PTFE/CNTs mixture offers a simple method to adjust hydrophobic/hydrophilic performance, which plays a critical role for oxygen transfer through porous diffusion layer.

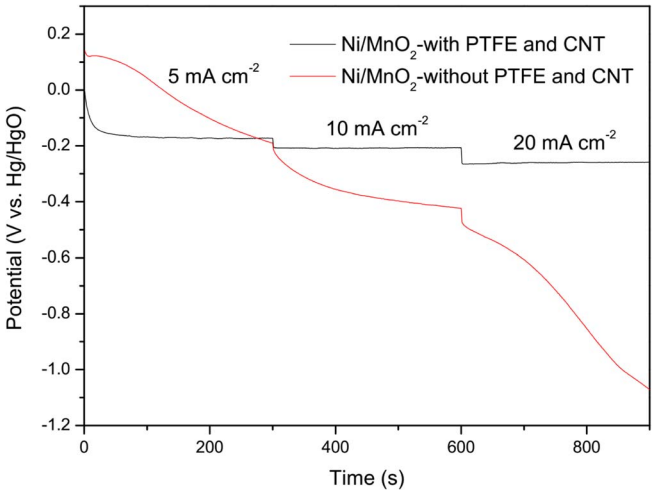

Figure 5. Comparison of ORR activity of MnO_2-coated Ni foam with PTFE:CNT (1:2) and without the mixture.

After the hydrothermal process, the surface of nickel foam electrode covered by MnO_2 becomes hydrophilic, thus is easily wetted by water. The mixture of PTFE/CNTs has proper hydrophobicity and porosity, which ensure oxygen transfer through micro pores inside the electrode, and the liquid–gas–solid triphase reaction can be carried out smoothly. In contrast with the conventional ORR electrode, in which catalytic active layer is usually composed of the mixture of electrocatalyst and PTFE/carbon fine powder, this novel fabrication method provides a structure that MnO_2 directly grows on the porous nickel foam, and then the mixture of PTFE/CNTs is filled into nickel foam to form gas diffusion layer, thus leading to successfully increased active surface area, decreased dead volume and controlled multiphase interfaces. Therefore, this novel air electrode is fundamentally favorable for electron conductivity and triphase electrochemical reaction.

Effect of mass transfer behaviors on oxygen reduction performance.—To determine the relationship between the mass-transfer structure and oxygen reduction performance, galvanostatic discharge tests were conducted in a three-electrode half cell. Fig. 6a shows the potentials measured at different current densities for the MnO_2-coated Ni foam with different mass ratios of PTFE to CNTs. The sample with a PTFE:CNT mass ratio of 0:1 exhibited a low ORR activity compared with the samples with mass ratios of 1:2–4:1 because the electrode was easily flooded without PTFE, which can increase the hydrophobicity of the microstructure inside the electrode. With increasing PTFE content, the electrochemical activity decreased because ohmic resistance became the main barrier after the quantity of PTFE exceeded the optimum content. The potential difference increased with increasing current density from 5 to 30 mA cm^{-2}, as observed in the mass ratio range of 4:1–10:1. This finding can be explained by the mass-transfer restriction of oxygen and ohmic resistance increase with increasing current densities.

The different mass ratios of PTFE to CNTs result in different transfer structures, which affect the ORR activity. A pore size distribution diagram (Fig. 6b) was used to analyze the structure in more depth. The sample with a PTFE:CNT mass ratio of 1:2 contained more micropores than the sample without PTFE, with an increase in the quantity of

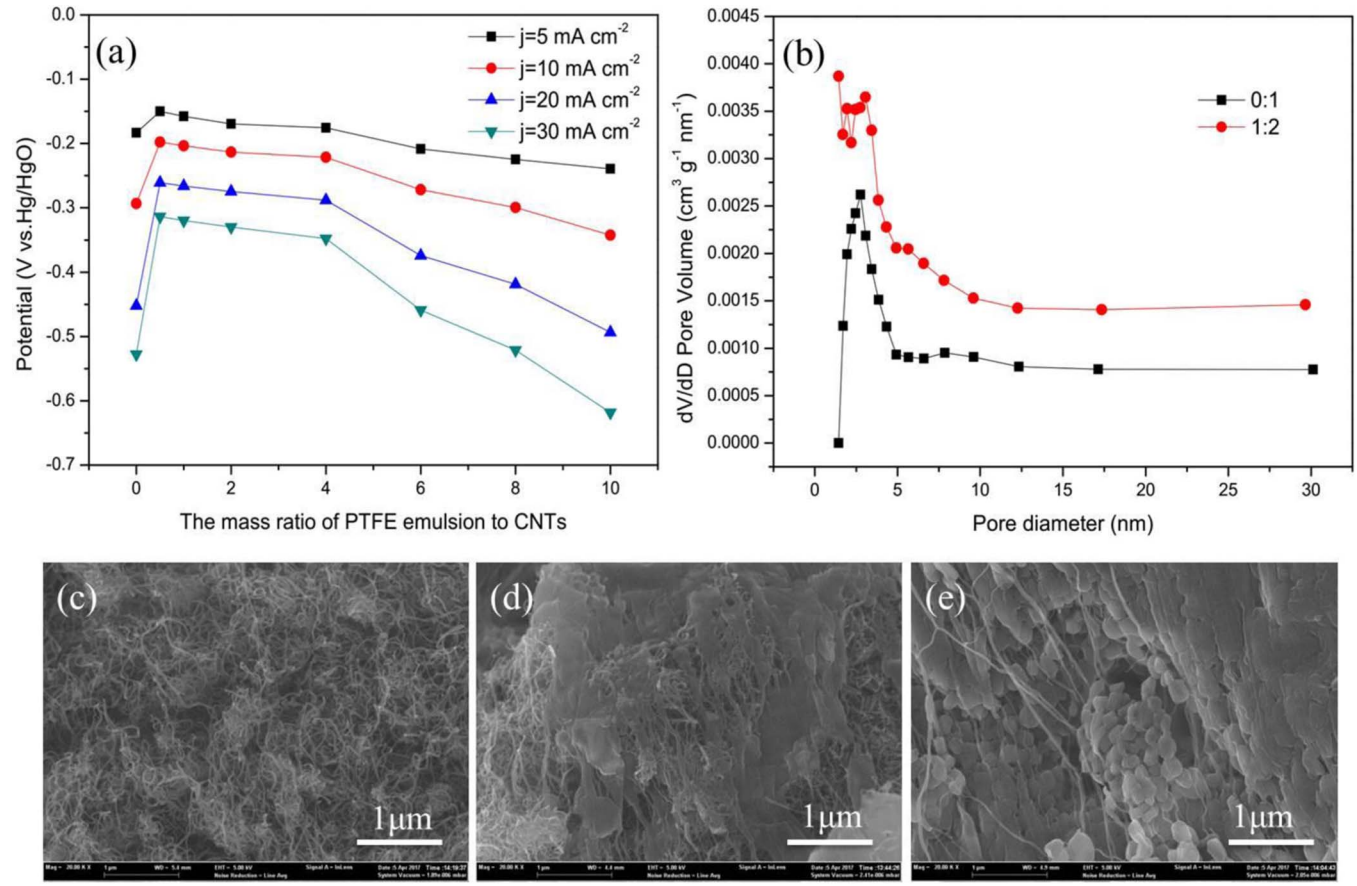

Figure 6. (a) Electrochemical activity of air cathodes using different mass ratios of PTFE to CNTs in 6 M KOH under ambient air atmosphere at 5, 10, 20, and 30 mA cm^{-2}. (b) Pore size distribution of air cathodes with different mass ratios of PTFE to CNTs (0:1, 1:2). FE-SEM images of cross-sections of air cathodes using mass ratios of PTFE to CNTs of (c) 1:2, (d) 4:1, and (e) 8:1.

Table I. Surface area, pore volume, and average pore diameter (N_2 adsorption–desorption isotherm) of air cathodes with different mass ratios of PTFE to CNTs.

PTFE:CNT[a]	Specific surface area ($m^2\ g^{-1}$)	Pore volume ($cm^3\ g^{-1}$)	Pore diameter (nm)
0:1	13.80	0.076	2.756
1:2	26.81	0.170	1.436
4:1	16.38	0.120	1.440
8:1	14.97	0.082	2.475

[a]PTFE:CNT is the mass ratio of the PTFE emulsion to CNTs.

pores with sizes of less than 5 nm promoting the mass-transfer process. The cross-sectional images show the high-magnification structures. As observed in Figs. 6c, 6d, 6e, the samples with PTFE:CNT mass ratios of 1:2, 4:1, and 8:1 consisted of mainly CNTs, a mixture of PTFE and CNTs, and more spherical PTFE, respectively. The inclusion of PTFE affected the hydrophobicity of the electrode and provided channels for gas transport around PTFE that promoted oxygen diffusion. However, for excessive PTFE contents, the catalyst particles could be coated with PTFE, resulting in decreased electron conductivity and low catalyst utilization.

Moreover, the BET results indicate that the Ni/MnO_2 with a PTFE:CNT mass ratio of 1:2 had the highest specific surface area of 26.81 $m^2\ g^{-1}$ (Table I), which is consistent with the trend observed in Fig. 6a. Here, PTFE acts as a spacer between different CNT agglomerates. Consequently, PTFE played an important role in this process, such as modifying the pore structure inside the electrode, altering the pore size in the micro system, and increasing the hydrophobicity.

EIS analysis and electrochemical active surface area.—The EIS analysis indicated that a suitable composition of PTFE was beneficial for oxygen transfer and reduction of the charge-transfer process. According to the Nyquist plots, the impedance spectra consisted of two semicircles in the high- and low-frequency regions. The first semicircle was related to the surface process between the electrode and electrolyte, and the second semicircle was related to the charge-transfer resistance of the electrode, which was directly related to the electrocatalytic activity of the air electrode. The impedance data were fitted using five elements, R_s, Q_{int}, R_{int}, Q_{dl}, and R_{ct}, and the resultant equivalent circuit is shown in Figure 7. A similar equivalent circuit has been proposed by other researchers for investigating the electrode processes of metal–air batteries.[35,39,41,73] The various resistances associated with the battery components, such as the electrolyte and contact resistances, are represented by R_s. The resistance arising from the solid-electrolyte interface is represented by R_{int}. The charge-transfer resistance encountered during the electrochemical reactions on the electrodes is represented by R_{ct}. The constant phase elements, Q_{int} and Q_{dl}, were incorporated into the equivalent circuit to represent the capacitances arising from the solid electrolyte interface on the air electrode. Figure 7 presents the impedance spectrum of Ni/MnO_2 with different mass ratios of PTFE to CNTs. The second semicircular diameter of Ni/MnO_2 with CNTs only was much larger than that of the other samples containing both PTFE and CNTs, implying a larger charge-transfer resistance. Table II summarizes the corresponding values of the equivalent circuit elements of different samples. R_{ct} first significantly decreased with increasing PTFE content and then increased. The R_{ct} values of Ni/MnO_2 without PTFE and with a PTFE:CNT mass ratio of 1:2 were 11.19 and 2.97 Ω, respectively, indicating that R_{ct} decreased significantly. Thereafter, with increasing PTFE content, R_{ct} increased from 3.4 to 14.94 Ω for increasing PTFE:CNT mass ratios from 2:1 to 10:1, respectively.

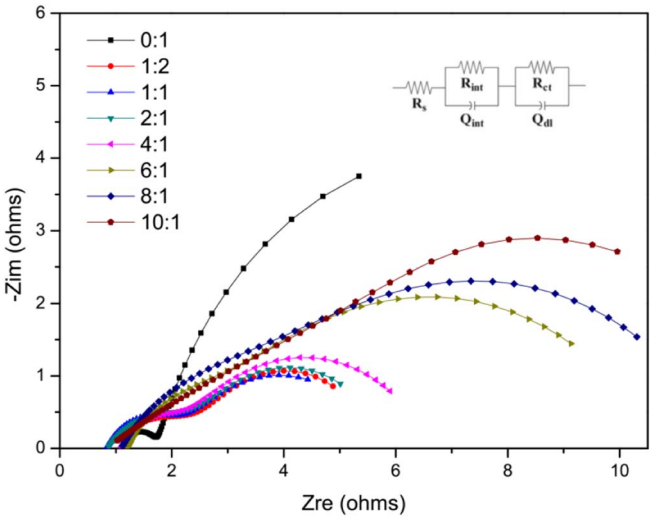

Figure 7. (a) EIS analysis of air cathodes using different mass ratios of PTFE to CNTs.

Moreover, C_{dl} measurements were conducted to estimate the electrochemical active surface area.[74–76] Figs. 8a, 8b shows the C_{dl} of Ni/MnO_2 with a mass ratio of PTFE to CNTs of 1:2 as an example. The current density exhibited a linear relationship with the scan rate, and C_{dl} was 223.1 mF cm^{-2}, which is higher than that of the electrodes with PTFE:CNT ratios ranging from 2:1 to 8:1 and with CNTs only (Table III), indicating a larger electrochemical active surface area. Oxygen reduction occurs at a three-phase interface and requires enough hydrophobic channels in the electrode for O_2 to pass through. The PTFE:CNT mass ratios of 1:4, 1:2, and 1:1 resulted in the best mass transfer structure inside the electrode with significantly larger electrochemical surface areas.

Effect of ni foam thickness on oxygen reduction performance.—The effect of the thickness of the primary Ni foam on the performance of the oxygen reduction electrode is shown in Figs. 9a, 9b. As observed in Fig. 9a, the air electrode with 3-mm-thick primary Ni foam exhibited the optimal oxygen reduction activity. The electrochemical activity was reduced upon further increasing the Ni foam thickness. This result was observed because the final thickness of the air electrode increased with increasing initial thickness of the primary Ni

Table II. Values of equivalent circuit elements based on EIS analysis of Ni/MnO_2 air electrodes with different mass ratios of PTFE to CNTs.

	PTFE:CNT[a]							
Element	0:1	1:2	1:1	2:1	4:1	6:1	8:1	10:1
$R_s(\Omega)$	1.12	0.832	0.848	0.86	1.098	1.194	1.095	0.833
$R_{int}(\Omega)$	0.62	1.87	1.35	1.64	1.11	1.54	2.56	1.97
$R_{ct}(\Omega)$	11.19	2.97	3.64	3.4	4.46	8.04	8.35	14.94
$Q_{int}(S \cdot s^n)$	0.0046	0.0261	0.0127	0.02	0.0085	0.011	0.0135	0.2341
$Q_{dl}(S \cdot s^n)$	0.2111	0.2203	0.2463	0.1864	0.0876	0.0543	0.0514	0.0661

[a]PTFE:CNT is the mass ratio of the PTFE emulsion to CNTs.

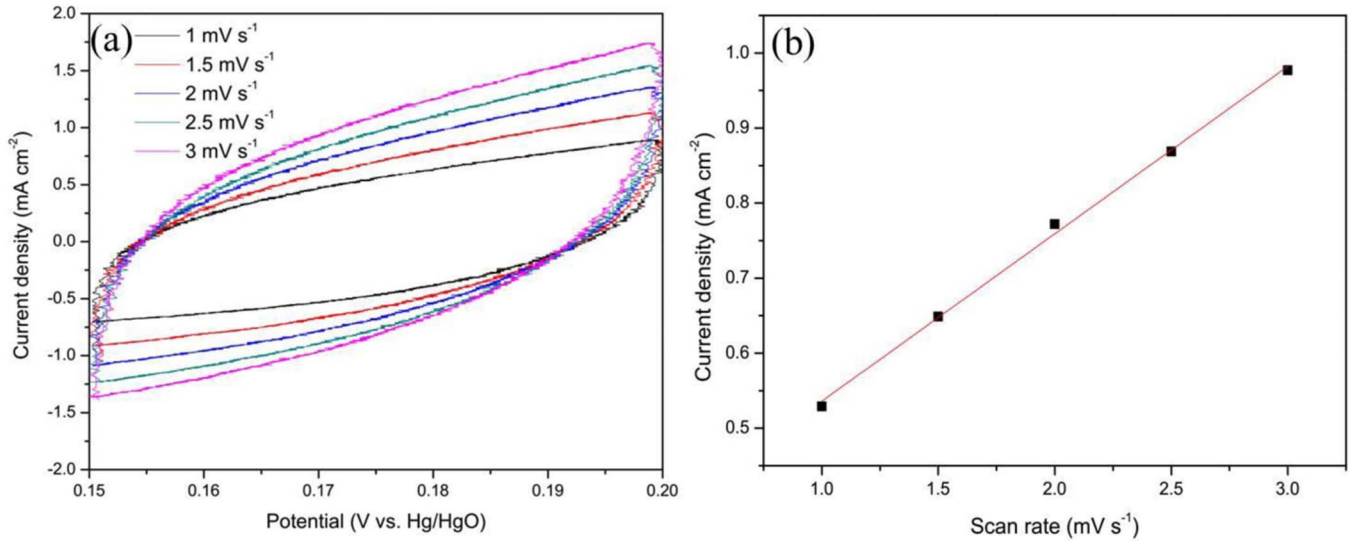

Figure 8. (a) CV curves of Ni/MnO_2 with mass ratio of PTFE to CNTs of 1:2 at scan rates of 1, 1.5, 2, 2.5, and 3 mV s^{-1}. (b) Linear relationship between current density and scan rate.

Table III. C_{dl} values of Ni/MnO_2 with different mass ratios of PTFE to CNTs.

PTFE:CNT[a]	0:1	1:4	1:2	1:1	2:1	4:1	6:1	8:1
C_{dl} (mF cm^{-2})	182.8	225.8	223.1	260.5	170.1	93.3	75.1	56.3

[a]PTFE:CNT is the mass ratio of PTFE emulsion to CNTs.

Table IV. Values of equivalent circuit elements based on EIS analysis of Ni/MnO_2 air electrodes with different Ni foam thicknesses.

	The thickness of Ni foam				
Element	1.7 mm	3 mm	5 mm	10 mm	15 mm
$R_s(\Omega)$	0.918	1.028	0.848	0.915	0.988
$R_{int}(\Omega)$	1.26	0.31	1.35	0.76	0.65
$R_{ct}(\Omega)$	4.94	3.50	3.64	6.82	8.54
$Q_{int}(S \cdot s^n)$	0.0843	0.1721	0.0127	0.0063	0.0043
$Q_{dl}(S \cdot s^n)$	0.0151	0.0043	0.2463	0.0404	0.0310

foam under the same compression pressure and because the relatively more hydrophilic catalyst loading per unit area resulted in a poor oxygen mass-transfer process. Furthermore, the loading of the hydrophilic catalyst was slightly less for the 1.7-mm-thick Ni foam for the same hydrophobic agents with a mass ratio of PTFE to CNTs of 1:1. The semicircular diameter of the Nyquist plot of the 15-mm-thick Ni foam was the largest of all the samples, suggesting the highest R_{ct} (Fig. 9b). Fig. 9b and Table IV show that the 3-mm-thick Ni foam had a R_{ct} of 3.5 Ω, which is significantly smaller than that of the 10-mm-thick Ni foam (6.82 Ω). This result is attributed to the enhanced transfer of charge and greater active material utilization during the electrochemical reaction. In addition, R_{int} of the 3-mm-thick electrode was 0.31 Ω, which is much lower than that for the other thicknesses, indicating much lower interfacial resistance between the electrode and electrolyte. The 3-mm-thick Ni foam with the appropriate hydrophilic catalyst loading exhibited a better balance between the hydrophilicity

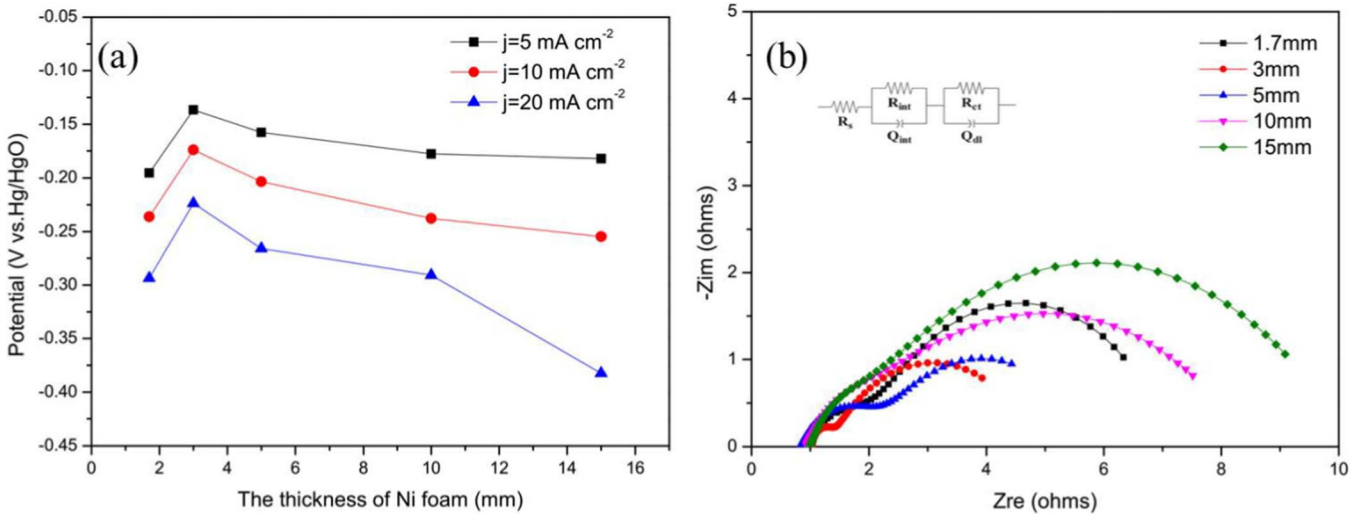

Figure 9. (a) Electrochemical activity of air cathodes for different thicknesses of Ni foam in 6 M KOH under ambient air atmosphere at 5, 10, and 20 mA cm^{-2}. (b) EIS analysis of air cathodes using different Ni foam thicknesses with a mass ratio of PTFE to CNTs of 1:1.

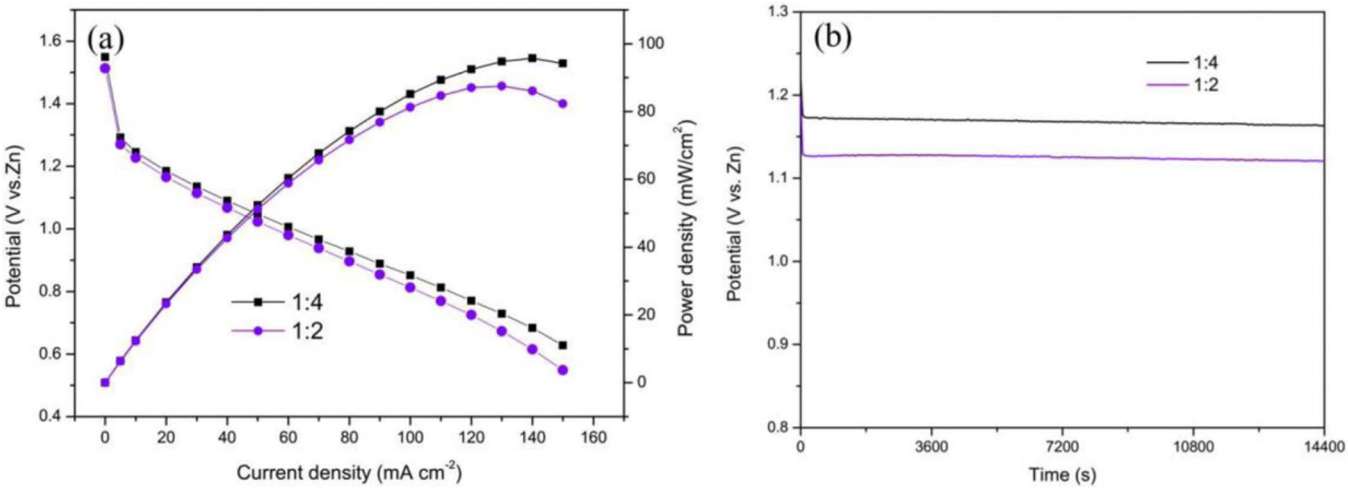

Figure 10. (a) Discharge curves and power densities of zinc–air batteries with air cathodes made of 3-mm-thick Ni foam using different mass ratios of PTFE to CNTs (1:4, 1:2) in 6 M KOH under ambient air atmosphere. (b) Discharge curves of zinc–air batteries with air cathodes composed of different mass ratios of PTFE to CNTs (1:4, 1:2) at a current density of 20 mA cm^{-2}.

and hydrophobicity than the Ni foams of other thicknesses. It can thus be concluded that with increasing Ni foam thickness, the loading of the catalyst increases, contributing to improved performance. However, for thicknesses greater than the optimal thickness, the increase in the mass-transfer resistance causes poor performance. Therefore, the electrode with optimal thickness is one that can achieve the best balance between the catalyst loading and mass-transfer resistance.

Zinc–air battery performance.—Ni foam with the optimal thickness of 3 mm was used as the substrate of the air electrode for zinc–air battery tests. Fig. 10 shows the performance of air electrodes with PTFE:CNT mass ratios of 1:4 and 1:2 used in zinc–air batteries. The discharge curves and power density curves are presented in Fig. 10a. Ni/MnO_2-1:4 had a 0.8-V discharge voltage at a current density of 100 mA cm^{-2}, with a power density of more than 80 mW cm^{-2} at a current density of 100 mA cm^{-2}. The peak power density of Ni/MnO_2-1:4 was 95.7 mW cm^{-2}, which is better than that of other Mn catalyst-based electrodes in the literature[41,57,77,78] (Table V). Fig. 10b shows the stability of two types of electrodes at a current density of 20 mA cm^{-2}. The Ni/MnO_2-1:4 electrode had a 1.18-V discharge voltage at a current density of 20 mA cm^{-2}. Moreover, no obvious potential change was observed during 14400-s tests, indicating that the technology of MnO_2 catalysts directly grown on Ni foam is feasible for oxygen reduction application.

Table V. Comparison of open-circuit voltage and peak power density of different manganese-based catalysts used in primary zinc–air batteries reported in the literature.

Catalyst	Substrate	Open Circuit voltage (V)	Peak power density (mW cm^{-2})	Reference
MnO_2-1:4	Ni foam	1.55	95.7	This work
MnO_2-1:2	Ni foam	1.51	87.5	This work
α-MnO_2	Carbon paper	1.45	61.5	77
MnO_2/$LaNiO_3$/CNT	Ni mesh	NA	55.0	57
MnO_x powder	Carbon paper	1.50	48.0	41
MnO_2 nanotubes	Carbon paper	1.55	36.0	78
MnO_2/Co_3O_4	Carbon paper	1.50	33.0	78

Conclusions

Oxygen reduction electrodes were improved by the design of the oxygen transfer route inside Ni foam coated with MnO_2 electrocatalysts using hydrothermal synthesis. To enhance the oxygen transport, optimal PTFE:CNT mass ratios in the range of 1:4–2:1 were adopted, which achieved the most efficient balance between the hydrophilic/hydrophobic interface with relatively larger electrochemical active area, low resistance, and small pore size. Moreover, PTFE not only served as a hydrophobic agent but also helped modify the pore structure inside the gas diffusion electrode. This novel structure used in zinc–air batteries resulted in a peak power density of 95.7 mW cm^{-2}, which was attributed to the three-dimensional design of the electrode with smooth electron transport, sufficient access to catalytically active sites, and more efficient gas transport. Based on the time efficiency, ease of preparation, and high activity and stability of this novel air cathode, it has great potential for application in long-lifetime metal-air batteries and other electrochemical devices.

Acknowledgments

The authors gratefully acknowledge the financial support provided by the National Natural Science Foundation of China (21276134, 21776154) and the National 863 Project (2012AA051203).

ORCID

Baoguo Wang https://orcid.org/0000-0001-9075-3695

References

1. F. Cheng and J. Chen, *Chem. Soc. Rev.*, **41**, 2172 (2012).
2. J. Fu, Z. P. Cano, M. G. Park, A. Yu, M. Fowler, and Z. Chen, *Adv. Mater.*, **29**, 1604685 (2017).
3. J. S. Spendelow and A. Wieckowski, *Phys. Chem. Chem. Phys.*, **9**, 2654 (2007).
4. P. Christensen, A. Hamnett, and D. Linares-Moya, *Phys. Chem. Chem. Phys.*, **13**, 5206 (2011).
5. W. Vielstich, H. Yokokawa, and H. A. Gasteiger, *Handbook of fuel cells: fundamentals technology and applications*, John Wiley & Sons (2009).
6. L. Jörissen, *Journal of Power Sources*, **155**, 23 (2006).
7. W. F. Linke and A. Seidell, *Solubilities, Inorganic and Metal-organic Compounds, K-Z: A Compilation of Solubility Data from the Periodical Literature. A Revision and Continuation of the Compilation Originated by Atherton Seidell*, American Chemical Society (1965).
8. K. E. Gubbins and R. D. Walker, *Journal of The Electrochemical Society*, **112**, 469 (1965).
9. Y. G. Li and H. J. Dai, *Chem. Soc. Rev.*, **43**, 5257 (2014).
10. M. Shao, Q. Chang, J.-P. Dodelet, and R. Chenitz, *Chem. Rev.*, **116**, 3594 (2016).

11. W. Xia, A. Mahmood, Z. Liang, R. Zou, and S. Guo, *Angew. Chem. Int. Ed.*, **55**, 2650 (2016).
12. Z. L. Wang, D. Xu, J. J. Xu, and X. B. Zhang, *Chem. Soc. Rev.*, **43**, 7746 (2014).
13. X. Ge, A. Sumboja, D. Wuu, T. An, B. Li, F. W. T. Goh, T. S. A. Hor, Y. Zong, and Z. Liu, *ACS Catalysis*, **5**, 4643 (2015).
14. W. J. Jiang, L. Gu, L. Li, Y. Zhang, X. Zhang, L. J. Zhang, J. Q. Wang, J. S. Hu, Z. Wei, and L. J. Wan, *J. Am. Chem. Soc.*, **138**, 3570 (2016).
15. S. S. Shinde, C. H. Lee, A. Sami, D. H. Kim, S. U. Lee, and J. H. Lee, *ACS Nano*, **11**, 347 (2017).
16. X. Liu, M. Park, M. G. Kim, S. Gupta, X. Wang, G. Wu, and J. Cho, *Nano Energy*, **20**, 315 (2016).
17. D. U. Lee, P. Xu, Z. P. Cano, A. G. Kashkooli, M. G. Park, and Z. Chen, *J. Mater. Chem. A*, **4**, 7107 (2016).
18. Y. Xue, H. Miao, S. Sun, Q. Wang, S. Li, and Z. Liu, *Journal of Power Sources*, **342**, 192 (2017).
19. Q. Zhao, Z. Yan, C. Chen, and J. Chen, *Chemical Reviews*, **117**, 10121 (2017).
20. M. Prabu, K. Ketpang, and S. Shanmugam, *Nanoscale*, **6**, 3173 (2014).
21. Q. Liu, J. Jin, and J. Zhang, *ACS applied materials & interfaces*, **5**, 5002 (2013).
22. N. Alonso-Vante, *Electrocatalysis in Fuel Cells*, p. 417, Springer (2013).
23. D. H. Youn, G. Bae, S. Han, J. Y. Kim, J.-W. Jang, H. Park, S. H. Choi, and J. S. Lee, *Journal of Materials Chemistry A*, **1**, 8007 (2013).
24. M. Shen, C. Wei, K. Ai, and L. Lu, *Nano Research*, **10**,1449 (2017).
25. H. Cui, Z. Zhou, and D. Jia, *Mater. Horiz.*, **4**, 7 (2017).
26. C. Zhu, H. Li, S. Fu, D. Du, and Y. Lin, *Chem. Soc. Rev.*, **45**, 517 (2016).
27. Y. Zheng, Y. Jiao, Y. Zhu, Q. Cai, A. Vasileff, L. H. Li, Y. Han, Y. Chen, and S.-Z. Qiao, *J. Am. Chem. Soc.*, **139**, 3336 (2017).
28. H. Wu, H. Li, X. Zhao, Q. Liu, J. Wang, J. Xiao, S. Xie, R. Si, F. Yang, S. Miao, X. Guo, G. Wang, and X. Bao, *Energy Environ. Sci.*, **9**, 3736 (2016).
29. A. Pendashteh, J. Palma, M. Anderson, and R. Marcilla, *Applied Catalysis B: Environmental*, **201**, 241 (2017).
30. M. Prabu, P. Ramakrishnan, and S. Shanmugam, *Electrochemistry Communications*, **41**, 59 (2014).
31. A. Loh, K. Xu, X. Li, and B. Wang, *Electrochimica Acta*, **245**, 615 (2017).
32. N. Xu, Y. Liu, X. Zhang, X. Li, A. Li, J. Qiao, and J. Zhang, *Sci. Rep.*, **6**, 33590 (2016).
33. G. Li, X. Wang, J. Fu, J. Li, M. G. Park, Y. Zhang, G. Lui, and Z. Chen, *Angew. Chem. Int. Ed.*, **55**, 4977 (2016).
34. J. Wang, H. Wu, D. Gao, S. Miao, G. Wang, and X. Bao, *Nano Energy*, **13**, 387 (2015).
35. J. Fu, F. M. Hassan, J. Li, D. U. Lee, A. R. Ghannoum, G. Lui, M. A. Hoque, and Z. Chen, *Adv. Mater.*, **28**, 6421 (2016).
36. J. W. D. Ng, M. Tang, and T. F. Jaramillo, *Energy & Environmental Science*, **7**, 2017 (2014).
37. T. Y. Ma, J. Ran, S. Dai, M. Jaroniec, and S. Z. Qiao, *Angew. Chem. Int. Ed.*, **54**, 4646 (2015).
38. B. Li, X. Ge, F. W. Goh, T. S. Hor, D. Geng, G. Du, Z. Liu, J. Zhang, X. Liu, and Y. Zong, *Nanoscale*, **7**, 1830 (2015).
39. D. U. Lee, J.-Y. Choi, K. Feng, H. W. Park, and Z. Chen, *Advanced Energy Materials*, **4**, 1301389 (2014).
40. F. Meng, H. Zhong, D. Bao, J. Yan, and X. Zhang, *J. Am. Chem. Soc.*, **138**, 10226 (2016).
41. A. Sumboja, X. Ge, F. W. T. Goh, B. Li, D. Geng, T. S. A. Hor, Y. Zong, and Z. Liu, *ChemPlusChem*, **80**, 1341 (2015).
42. Y. Xu, Y. Zhang, Z. Guo, J. Ren, Y. Wang, and H. Peng, *Angew. Chem. Int. Ed.*, **54**, 15390 (2015).
43. X. Wu, F. Chen, Y. Jin, N. Zhang, and R. L. Johnston, *ACS Appl. Mater. Interfaces*, **7**, 17782 (2015).
44. S. Chen, J. Duan, P. Bian, Y. Tang, R. Zheng, and S.-Z. Qiao, *Advanced Energy Materials*, **5**, 1500936 (2015).
45. B. Li, J. Quan, A. Loh, J. Chai, Y. Chen, C. Tan, X. Ge, T. S. Hor, Z. Liu, H. Zhang, and Y. Zong, *Nano Lett.*, **17**, 156 (2017).
46. X. Wu, F. Chen, N. Zhang, A. Qaseem, and R. L. Johnston, *Small*, **13**, 1603876 (2017).
47. X. Wu, F. Chen, N. Zhang, A. Qaseem, and R. L. Johnston, *J. Mater. Chem. A*, **4**, 3527 (2016).
48. M. Yu, Z. Wang, C. Hou, Z. Wang, C. Liang, C. Zhao, Y. Tong, X. Lu, and S. Yang, *Adv. Mater.*, **29**, 1602868 (2017).
49. P. Wang, T. Hayashi, Q. Meng, Q. Wang, H. Liu, K. Hashimoto, and L. Jiang, *Small*, **13**, 1601250 (2017).
50. Y. Lei, R. Sun, X. Zhang, X. Feng, and L. Jiang, *Adv. Mater.*, **28**, 1477 (2016).
51. Z. Lu, M. Sun, T. Xu, Y. Li, W. Xu, Z. Chang, Y. Ding, X. Sun, and L. Jiang, *Adv. Mater.*, **27**, 2361 (2015).
52. Y. Wu, K. Liu, B. Su, and L. Jiang, *Adv. Mater.*, **26**, 1124 (2014).
53. H. Wang, J. Zhang, X. Hang, X. Zhang, J. Xie, B. Pan, and Y. Xie, *Angew. Chem. Int. Ed.*, **127**, 1211 (2015).
54. K. Zhang, X. Han, Z. Hu, X. Zhang, Z. Tao, and J. Chen, *Chem. Soc. Rev.*, **44**, 699 (2015).
55. I. M. Mosa, S. Biswas, A. M. El-Sawy, V. Botu, C. Guild, W. Song, R. Ramprasad, J. F. Rusling, and S. L. Suib, *J. Mater. Chem. A*, **4**, 620 (2016).
56. T. Takashima, K. Hashimoto, and R. Nakamura, *J. Am. Chem. Soc.*, **134**, 1519 (2012).
57. H. Ma and B. Wang, *RSC Adv.*, **4**, 46084 (2014).
58. W. Hong, *International Journal of Electrochemical Science*, **11**, 3843 (2016).
59. Y. Meng, W. Song, H. Huang, Z. Ren, S. Y. Chen, and S. L. Suib, *J. Am. Chem. Soc.*, **136**, 11452 (2014).
60. F. Cheng, T. Zhang, Y. Zhang, J. Du, X. Han, and J. Chen, *Angew. Chem. Int. Ed.*, **52**, 2474 (2013).
61. Y. X. Zhao, C. Chang, F. Teng, Y. F. Zhao, G. B. Chen, R. Shi, G. I. N. Waterhouse, W. F. Huang, and T. R. Zhang, *Advanced Energy Materials*, **7**, 1700005 (2017).
62. A. C. Thenuwara, E. B. Cerkez, S. L. Shumlas, N. H. Attanayake, I. G. McKendry, L. Frazer, E. Borguet, Q. Kang, R. C. Remsing, and M. L. Klein, *Angew. Chem. Int. Ed.*, **55**, 10381 (2016).
63. M. Huang, X. L. Zhao, F. Li, L. L. Zhang, and Y. X. Zhang, *Journal of Power Sources*, **277**, 36 (2015).
64. B. A. Pinaud, Z. Chen, D. N. Abram, and T. F. Jaramillo, *The Journal of Physical Chemistry C*, **115**, 11830 (2011).
65. M. Oku, K. Hirokawa, and S. Ikeda, *Journal of Electron Spectroscopy and Related Phenomena*, **7**, 465 (1975).
66. P. Lv, Y. Y. Feng, Y. Li, and W. Feng, *Journal of Power Sources*, **220**, 160 (2012).
67. V. Di Castro and G. Polzonetti, *Journal of Electron Spectroscopy and Related Phenomena*, **48**, 117 (1989).
68. S. Sopčić, R. Peter, M. Petravić, and Z. Mandić, *Journal of Power Sources*, **240**, 252 (2013).
69. M. Toupin, T. Brousse, and D. Bélanger, *Chemistry of Materials*, **16**, 3184 (2004).
70. F. Cheng, Y. Su, J. Liang, Z. Tao, and J. Chen, *Chemistry of Materials*, **22**, 898 (2009).
71. M. Lu, S. Kharkwal, H. Y. Ng, and S. F. Y. Li, *Biosensors and Bioelectronics*, **26**, 4728 (2011).
72. Y. Liang, Y. Li, H. Wang, J. Zhou, J. Wang, T. Regier, and H. Dai, *Nat. Mater.*, **10**, 780 (2011).
73. Z. Chen, A. Yu, D. Higgins, H. Li, H. Wang, and Z. Chen, *Nano Lett.*, **12**, 1946 (2012).
74. T. Y. Ma, S. Dai, M. Jaroniec, and S. Z. Qiao, *J. Am. Chem. Soc.*, **136**, 13925 (2014).
75. K. Li, J. Zhang, R. Wu, Y. Yu, and B. Zhang, *Adv. Sci.*, **3**, 1500426 (2016).
76. J. Tian, Q. Liu, A. M. Asiri, and X. Sun, *J. Am. Chem. Soc.*, **136**, 7587 (2014).
77. P.-C. Li, C.-C. Hu, H. Noda, and H. Habazaki, *Journal of Power Sources*, **298**, 102 (2015).
78. G. Du, X. Liu, Y. Zong, T. S. Hor, A. Yu, and Z. Liu, *Nanoscale*, **5**, 4657 (2013).